

# The Mass Distribution of CL0939+4713 obtained from a ‘Weak’ Lensing Analysis of a WFPC2 image

Carolyn Seitz<sup>1</sup>, Jean-Paul Kneib<sup>2</sup>, Peter Schneider<sup>1</sup> & Stella Seitz<sup>1</sup>

<sup>1</sup> Max-Planck-Institut für Astrophysik, Postfach 1523, D-85740 Garching, Germany.

<sup>2</sup> Institute of Astronomy, Madingley Road, Cambridge CB3 0HA, UK.

## Abstract

The image distortions of high-redshift galaxies caused by gravitational light deflection of foreground clusters of galaxies can be used to reconstruct the two-dimensional surface mass density of these clusters. We apply an unbiased parameter-free reconstruction technique to the cluster CL0939+4713 (Abell 851), observed with the WFPC2 on board of the HST. We demonstrate that a single deep WFPC2 observation can be used for cluster mass reconstruction despite its small field of view and the irregular shape of the data field (especially for distant clusters). For CL0939, we find a strong correlation between the reconstructed mass distribution and the bright cluster galaxies indicating that mass follows light on average. The detected anti-correlation between the faint galaxies and the reconstructed mass is most likely an effect of the magnification (anti) bias, which was detected previously in the cluster A1689. Because of the high redshift of CL0939 ( $z_d = 0.41$ ), the redshift distribution of the lensed, faint galaxies has to be accounted for in the reconstruction technique. We derive an approximate global transformation for the surface mass density which leaves the mean image ellipticities invariant, resulting in an uncertainty in the normalization of the mass. From the non-negativity of the surface mass density, we derive lower limits on the mass inside the observed field of  $0.75(h_{50}^{-1} \text{ Mpc})^2$  ranging from  $M > 3.6 \times 10^{14} h_{50}^{-1} M_\odot$  to  $M > 6.3 \times 10^{14} h_{50}^{-1} M_\odot$  for a mean redshift of  $\langle z \rangle = 1$  to  $\langle z \rangle = 0.6$  of the faint galaxy images with  $R \in (23, 25.5)$ . However, we can break the invariance transformation for the mass using the magnification effect on the observed number density of the background galaxies. Assuming a mean redshift of  $\langle z \rangle = 0.8$  and a fraction of  $x = 15\%$  ( $x = 20\%$ ) of cluster galaxies in the observed galaxy sample with  $R \in (23, 25.5)$  we obtain for the mass inside the field  $M \approx 5 \times 10^{14} h_{50}^{-1} M_\odot$  ( $M \approx 7 \times 10^{14} h_{50}^{-1} M_\odot$ ) which corresponds to  $M/L \approx 100 h_{50}$  ( $M/L \approx 140 h_{50}$ ).

# 1. Introduction

Since the pioneering work of Tyson, Valdes and Wenk (1990) it has been realized that the weak shearing effects of clusters introduced on images of faint background galaxies can be used to obtain the mass distribution of these lensing clusters (for a recent review on cluster lensing, see Fort & Mellier 1994; see also Kochanek 1990; Miralda-Escudé 1991). Kaiser & Squires (1993, hereafter KS) have derived an explicit expression for the two-dimensional surface mass density as a function of the shear (or tidal gravitational field) caused by the cluster, which in turn can be obtained from the distorted images of background galaxies. This inversion method has been applied to several clusters observed from the ground (Fahlman et al. 1994, Smail et al. 1995a, Kaiser et al. 1995), demonstrating the applicability of this new method to determine mass profiles and total mass estimates of clusters. The detection of sheared images far out in the cluster 0024+16 (Bonnet, Mellier & Fort 1994; Kassiola et al. 1994) shows that weak lensing can investigate previously unexplored regions in clusters.

Recently, the KS inversion technique has been modified and generalized to account for strong lensing, as it should occur near the center of clusters (Schneider & Seitz 1995, Seitz & Schneider 1995a, Kaiser 1995), and for the finite data field defined by the CCD size (Schneider 1995, Kaiser et al. 1995, Bartelmann 1995, Seitz & Schneider 1995b, henceforth SS). In SS, a detailed quantitative comparison between the various inversion techniques has been made, and it was demonstrated that the inversion formula derived in SS is the most accurate of the unbiased ones. In particular, if the cluster mass distribution is significantly more extended than the data field (i.e. the CCD), the SS inversion formula is significantly more accurate than the other currently known inversion techniques.

Such a situation generally occurs if the data are taken with the WFPC2 on board the *Hubble Space Telescope* (HST), owing to its fairly small field of view. Hence, if WFPC2 images are used for the reconstruction of the surface mass density of a cluster, it is necessary to use a finite-field inversion formula such as the one derived in SS. As was pointed out in Schneider & Seitz 1995, even then the mass density can be derived only up to a global invariance transformation, which is the mass-sheet degeneracy found by Gorenstein et al. (1988). The invariance transformation may be broken if the magnification effects are taken into account which changes the local number density of images of an appropriately chosen subset of faint galaxies (Broadhurst, Taylor & Peacock 1995), and which changes the size of galaxy images at fixed surface brightness – which is unchanged by gravitational light deflection (Bartelmann & Narayan 1995). In particular, this latter paper demonstrates that the inclusion of magnification effects may improve the cluster mass inversion considerably, and can also provide a unique means to determine the redshift distribution down to very faint magnitudes.

In this paper we present the first application of a finite-field cluster inversion to the deep WFPC2 observation (10 orbits) of the distant cluster CL 0939+4713 retrieved from the HST archive. These data have been used for the study of the morphology of the cluster galaxies and the Butcher–Oemler effect by Dressler et al. (1994a). In Sect. 2 we briefly describe the data, and discuss the image identification and the determination of the image shapes, which is used for the estimate of the local image distortion. Sect. 3 briefly summarizes the inversion method, the results of which are presented in Sect. 4 and discussed in Sect. 5.

## 2. Observation and data analysis

**Fig. 1a.** Observations of the cluster CL0939+4713 obtained with WFPC2 using the 702W filter and an exposure time of 21000s. The side-length of the data field is  $2'.5$  ( $1h_{50}^{-1}$  Mpc) for an EdS-universe with  $H_0 = 50h_{50}$  km/s/Mpc, 1 arcsec on the sky represents  $6.51h_{50}^{-1}$  kpc). Dressler & Gunn (1992) propose the cluster center to be close to the 3 bright galaxies in the upper left corner of the lower left CCD. North is at the bottom east to the right

CL0939+4713 was observed in January 1994 with the WFPC2 camera on the Hubble Space Telescope (Dressler et al. 1994a). The observation consists of 10 single orbits of 2100 seconds (or a total exposure time of 5h50min) and corresponds probably to the deepest cluster observation done with the HST/WFPC2. The exposures were divided into two groups of 5 with a shift of 10 pixel East and 20 pixels South between the two groups. After StSci pipeline processing, the data were shifted and combined to remove cosmic rays and hot pixel using standard STSDAS/IRAF routines. A mosaic of the 3 WFC chips and the PC chips was constructed, though due to the smaller pixel size of the PC chip and therefore a brighter isophotal limit we discard it from the analysis. The image was then run through the SExtractor package (Bertin & Arnouts 1995) to detect objects, measure their magnitudes, mean isophotal surface brightness and second moments. All objects with isophotal areas larger than 12 pixels and higher than  $2\sigma$ /pixel

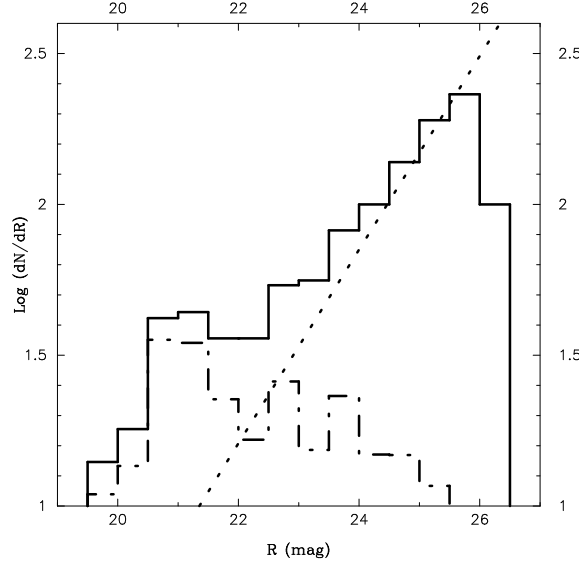
( $\mu_{F702W} = 25.3 \text{ mag/arcsec}^2$ ) were selected. For each object the unweighted first and second moments were computed to determine their center, their size, their ellipticity and orientation. To convert instrumental F702W magnitudes into standard  $R$  we use the synthetic zero point and color corrections listed in Holtzman et al. (1995). For the color term we choose  $(V - R) \simeq 0.6$  typical of a  $z \sim 0.8$  late-type spiral. The color correction is then  $+0.2 \text{ mag}$ , and remains small for other choices of the colour term. The typical photometric errors of our faintest objects,  $R < 26.5$ , are  $\delta R \sim 0.1\text{--}0.2$ . A neural network algorithm was used to identify stellar objects, 22 of those were detected. A galaxy catalogue was then constructed with a total of 572 galaxies down to  $R=26.5$ .

Fig. 1a shows the full WFPC2 image of the cluster, and Fig. 1b a zoomed image of the region marked in Fig. 1a. A detailed inspection discovered the arc candidate and a likely pair in this central cluster region. These strong lensing features confirm that the cluster is over-critical and probably indicate the densest part of the cluster. The spectroscopic observation of the bright pair ( $R=22.5$ , and  $R=22.9$  for it's counter-image candidate) will confirm or otherwise the lensing assumption. If it is indeed a gravitational pair, it will constrain strongly the mass distribution of the very central part of the cluster.

**Fig. 1b.** A zoomed image of the region marked in Fig. 1a. We find an arc-candidate A0 and a likely gravitational pair P1& 2 with the counter image P3

Fig. 2 shows the number vs. magnitude diagram of the galaxies detected in the field (solid line). These numbers are compared with the field galaxies counts in the  $R$  band

from Smail et al (1995b). It is clear that most of the galaxies with  $R \in (19, 22)$  are likely cluster members. Furthermore there is a likely contamination from cluster members of  $\sim 150$  objects down to  $R = 25.5$  within the WFC field; the cluster contamination is expected to be higher in the central part than in the outer part.



**Fig. 2.** The number vs. magnitude diagram of all galaxies detected within the WFC field (solid line). The dotted line shows the number counts – rescaled to the area of WFC field – from Smail et al. (1995b), which yields  $N(R) \propto 10^{\gamma R}$ , with  $\gamma = 0.32$  and normalization such that  $N(R < 27) = 7.3 \times 10^5$  per square degree. Assuming that the dotted line represents the counts of the faint galaxies, the dashed-dotted histogram gives the number counts versus magnitude of the cluster galaxies

From the second moments of light  $Q_{ij}$  we calculate for each galaxy image the (complex) ellipticity

$$\chi = \frac{Q_{11} - Q_{22} + 2iQ_{12}}{Q_{11} + Q_{22}} = |\chi| e^{2i\vartheta} . \quad (2.1a)$$

However, it is more convenient to work in terms of the ellipticity parameter  $\epsilon$  which has the same phase  $\theta$  as  $\chi$ , and modulus

$$|\epsilon| = \frac{1 - r}{1 + r} \quad \text{with} \quad r = \sqrt{\frac{1 - |\chi|}{1 + |\chi|}} . \quad (2.1b)$$

Then we use these image ellipticities  $\epsilon_k$  of a galaxy at  $\theta_k$  to calculate the local mean image ellipticity on a grid  $\theta_{ij}$

$$\bar{\epsilon}(\theta_{ij}) = \frac{\sum_{k=1}^{N_{\text{gal}}} \epsilon_k u(|\theta_{ij} - \theta_k|)}{\sum_{k=1}^{N_{\text{gal}}} u(|\theta_{ij} - \theta_k|)} , \quad (2.2)$$

with the weight factor

$$u(d) = \exp(-d^2/s^2) ,$$

with a smoothing length  $s$ , which, unless noted otherwise, is chosen as  $s = 0'.3$  ( $117 h_{50}^{-1}$  kpc). The resulting map of  $\bar{\epsilon}(\theta)$  is shown in Fig.3 using all images covering more

than 12 pixels (pixel-size  $0''.1$ ) and using four different magnitude cuts for the galaxies:  $R \in (24, 25.5)$  for the upper left panel,  $R \in (23, 25.5)$  for the upper right,  $R \in (22, 25.5)$  for the lower left and  $R \in (21, 25.5)$  for the lower right. The corresponding numbers of galaxies used for constructing the shear maps are 226, 295, 343, and 383, respectively, meaning that the average number of galaxies having a distance of less than the smoothing length from the point  $\theta_{ij}$  is about 13, 17, 20 and 22. The cut at fainter magnitude was chosen in order to be not too much contaminated by the circularization effect of measuring small galaxies with poor signal to noise. We find that the “shear field” is quite robust under adding brighter galaxies to the sample: the direction of the local shear vector is almost unchanged and its absolute value is decreased on average for the brighter galaxy samples, especially in regions close to the cluster center. The reason for this is that the modulus of the expectation value of the mean image ellipticities is smaller for background galaxies closer to the cluster and it is zero for cluster- and foreground galaxies, both leading to a decrease in the mean image ellipticities for the brighter galaxy samples. The direction of the expectation value of the mean image ellipticities is not changed, since the mean image orientation of the background galaxies does not depend on their distances to the cluster, and since cluster- and foreground galaxies show no preferred alignment at all.

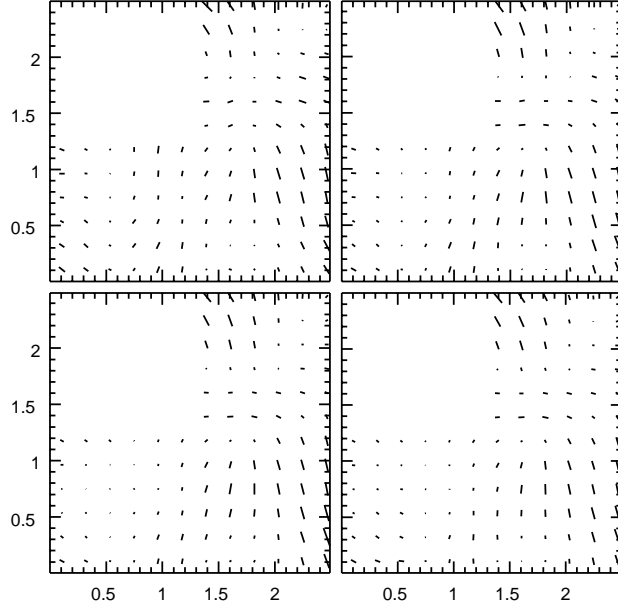


**Fig. 3.** The orientation and absolute value of the local mean image ellipticities  $\bar{e} = |\bar{e}| (\cos 2\varphi + i \sin 2\varphi)$  of galaxies with  $R \in (24, 25.5)$  (upper left),  $R \in (23, 25.5)$  (upper right),  $R \in (22, 25.5)$  (lower left) and  $R \in (21, 25.5)$  (lower right). We exclude galaxies covering less than 12 pixels (pixel-size  $0''.1$ ). We choose a smoothing length of  $s = 0''.3$ ; as is clearly seen, the ‘coherence length’ of the shear pattern is larger than this smoothing length. The vectors displayed include an angle of  $\varphi$  with the x-axis, and a mean image ellipticity  $|\bar{e}| = 1$  would correspond to a vector of length  $0.4$ .

### 3. Method of Reconstruction

In this section we briefly describe the reconstruction of the cluster surface mass density using the observed map of mean image ellipticities. Due to the high redshift of the cluster ( $z_d = 0.41$ ) we can not assume that all source galaxies are at the same effective distance to the cluster, i.e. that their  $D(z_d, z)/D(z)$  is the same. Therefore, we relate the critical surface mass density

$$\Sigma_{\text{crit}}(z) = \frac{c^2 D(z)}{4\pi G D(z_d) D(z_d, z)}$$

for a source at redshift  $z$  to the critical surface mass density for a source at ‘infinity’ by defining  $w(z)$  through

$$w(z) \Sigma_{\text{crit}}(z) = \lim_{z \rightarrow \infty} \Sigma_{\text{crit}}(z) ,$$

for  $z > z_d$ , and  $w(z) = 0$  for  $z \leq z_d$ , and obtain for the dimensionless surface mass density  $\kappa(\boldsymbol{\theta}, z)$  and the shear  $\gamma(\boldsymbol{\theta}, z)$

$$\kappa(\boldsymbol{\theta}, z) = w(z) \kappa_{\infty}(\boldsymbol{\theta}) \quad , \quad \gamma(\boldsymbol{\theta}, z) = w(z) \gamma_{\infty}(\boldsymbol{\theta}) \quad . \quad (3.1)$$

The form of  $w(z)$  depends on the geometry of the universe, and for an Einstein-de Sitter universe we have

$$w(z) = \begin{cases} 0 & \text{for } z \leq z_d; \\ \frac{\sqrt{1+z} - \sqrt{1+z_d}}{\sqrt{1+z} - 1} & \text{for } z > z_d. \end{cases} \quad (3.2)$$

The following description of the reconstruction of the surface mass density is based on the simplifying assumption that the cluster is not critical, i.e.,  $(1 - w\kappa_{\infty})^2 - w^2\gamma_{\infty}^2 > 0$  for all sources. However, we point out that all the resulting mass maps shown in this paper have been calculated *without* this assumption, using the more complicated method described in Seitz & Schneider (1995c). However, since the reconstruction is much easier to describe for non-critical clusters, we describe here the reconstruction of non-critical clusters only. We also note that there are only minor changes in the results if this assumption is introduced.

As described in Seitz & Schneider (1995c), the local expectation value of the image ellipticity can be approximated through

$$\langle \epsilon \rangle \approx \frac{-\langle w \rangle \gamma_{\infty}}{1 - f \langle w \rangle \kappa_{\infty}} , \quad (3.3)$$

if  $\kappa_{\infty} \lesssim 0.8$  and if the mean redshift of the sources is  $\langle z \rangle \gtrsim 0.7$  for this particular cluster redshift. In (3.3) we used the definitions

$$\langle w^k \rangle = \int_0^{\infty} dz p_s(z) w^k(z) \quad \text{and} \quad f = \frac{\langle w^2 \rangle}{\langle w \rangle^2} , \quad (3.4)$$

where  $p_s(z)$  is the redshift distribution of the sources. From (3.3) we find that the transformation  $\kappa_{\infty} \rightarrow \kappa'_{\infty}$  with

$$\lambda \left( 1 - \kappa_{\infty} \frac{\langle w^2 \rangle}{\langle w \rangle} \right) = \left( 1 - \kappa'_{\infty} \frac{\langle w^2 \rangle}{\langle w \rangle} \right) \quad (3.5)$$

which implies that  $\gamma'_\infty = \lambda\gamma_\infty$ , leaves the image ellipticities unchanged. Therefore, using only image ellipticities for the reconstruction,  $1 - f \langle w \rangle \kappa_\infty$  can be derived only up to a multiplicative constant. Using the relation between the gradient of the surface mass density and the derivatives of the shear (Kaiser 1995), we obtain from (3.3) with  $K(\boldsymbol{\theta}) := \ln[1 - f \langle w \rangle \kappa_\infty(\boldsymbol{\theta})]$

$$\nabla K = \frac{1}{1 - f^2 |\langle \epsilon \rangle|^2} \begin{pmatrix} 1 - f \langle \epsilon_1 \rangle & -f \langle \epsilon_2 \rangle \\ -f \langle \epsilon_2 \rangle & 1 + f \langle \epsilon_1 \rangle \end{pmatrix} \begin{pmatrix} -f \langle \epsilon_1 \rangle_1 - f \langle \epsilon_2 \rangle_2 \\ -f \langle \epsilon_2 \rangle_1 + f \langle \epsilon_1 \rangle_2 \end{pmatrix} =: \mathbf{u}(\boldsymbol{\theta}) , \quad (3.6)$$

with  $\langle \epsilon \rangle = \langle \epsilon_1 \rangle + i \langle \epsilon_2 \rangle$  and gradients  $\langle \epsilon_i \rangle_j = \partial \langle \epsilon_i \rangle / \partial \theta_j$ . Since the mean image ellipticity  $\bar{\epsilon}$  provides an unbiased estimator of the expectation value  $\langle \epsilon \rangle$ , we set  $\langle \epsilon \rangle \approx \bar{\epsilon}$ . Then  $\mathbf{u}(\boldsymbol{\theta})$  can be determined from observations, for an assumed value of  $f$ , which characterizes the redshift distribution of the sources. From that,  $K(\boldsymbol{\theta})$  is obtained as

$$K(\boldsymbol{\theta}) = \int_{\mathcal{U}} d^2\theta' \mathbf{H}(\boldsymbol{\theta}, \boldsymbol{\theta}') \cdot \mathbf{u}(\boldsymbol{\theta}') + \bar{K} . \quad (3.7)$$

In Eq.(3.7), the kernel  $\mathbf{H}(\boldsymbol{\theta}, \boldsymbol{\theta}')$  is calculated for the data field  $\mathcal{U}$  according to the method suggested by Seitz & Schneider (1995b). So far we have not calculated the kernel  $\mathbf{H}$  for the irregularly-shaped WFPC2 field. Therefore, we reconstruct  $K$  on two rectangular fields with side-length of about  $2'.5 \times 1'.25$  and  $1'.25 \times 2'.5$ . Since we have an additive constant free, we shift one of the resulting  $K$ -maps such that the mean of  $K$  inside the overlapping region of the two data fields is the same. Then, the resulting mass map is obtained by joining together these two independent reconstructions at the diagonal of the lower right CCD. That means that all mass maps shown here display a discontinuity at this diagonal; however, the jump across this line is always remarkably small, indicating the relative uncertainty of the reconstruction.

The redshift distribution of the field galaxies down to the faint magnitude limits considered here is poorly known. Redshift surveys of considerably brighter galaxies indicate that the redshift distribution is fairly broad, and a high-redshift tail cannot be excluded (see Lilly 1993, Colless et al. 1993, and Cowie et al. 1995, and references therein). We therefore take the same parameterization of  $p_s(z)$  as used in Brainerd, Blandford & Smail (1995),

$$p_s(z) = \frac{\beta z^2}{\Gamma(3/\beta) z_0^3} \exp \left( - (z/z_0)^\beta \right) . \quad (3.8)$$

We consider different values of the parameter  $\beta$  for which the mean redshift is given through  $\langle z \rangle = z_0 \Gamma(4/\beta) / \Gamma(3/\beta)$ . In Fig. 4 we show the distribution  $p_s(z)$  for  $\beta = 1, 1.5, 3$  and  $\langle z \rangle \in \{0.8, 1.0, 1.5\}$  (right panels) and the moments  $\langle w \rangle$ ,  $\langle w^2 \rangle$  and  $f = \langle w^2 \rangle / \langle w \rangle^2$  as a function of the mean redshift  $\langle z \rangle$  for the redshift  $z_d = 0.41$  of CL 0939+4713 (left panels). Kneib et al. (1995) attempted using the Abell 2218 cluster-lens to determine the mean redshift distribution of the faint galaxies and found a mean value of  $\langle z \rangle \sim 0.8$  for  $23.5 < R < 25.5$  which is above but consistent with the non-evolution expectation. Therefore, our choice of the parametrization of the redshift distribution shall be close to the true distribution of faint galaxies.

## 4. Results



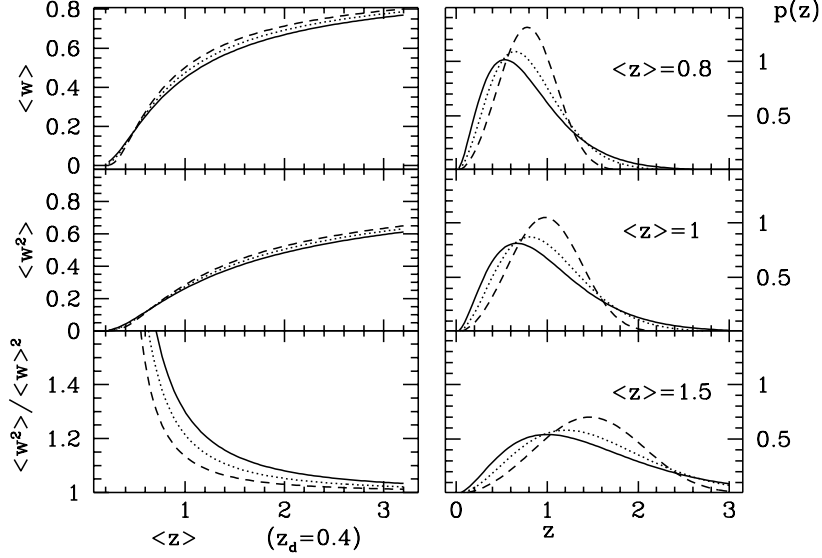


**Fig. 4.** The redshift distribution  $p_s(z)$ , defined in Eq. (3.8), is shown in the right panels for a mean redshift of  $\langle z \rangle = 0.8$  (top)  $\langle z \rangle = 1$  (middle) and  $\langle z \rangle = 1.5$  (bottom), and for the parameters  $\beta = 1$  (solid line),  $\beta = 1.5$  (dotted line) and  $\beta = 3$  (dashed line). The left panels show the moments  $\langle w \rangle$ ,  $\langle w^2 \rangle$  and the ratio  $f = \langle w^2 \rangle / \langle w \rangle^2$  defined in Eq. (3.4) as a function of mean redshift  $\langle z \rangle$  for a cluster redshift  $z_d = 0.4$

#### 4.1 The reconstructed mass distribution

In Fig.5 we show the reconstructed surface mass density for different mean redshifts  $\langle z \rangle$ , using in each case galaxies with  $R \in (23, 25.5)$  and the invariance transformation (3.5) such that the minimum of the resulting  $\kappa_\infty$ -map is roughly zero to avoid unphysical negative surface mass densities. We see that for a mean redshift of about  $\langle z \rangle = 0.6 - 0.8$  of the faint galaxies in this magnitude interval, the cluster is quite strong and could indeed be (marginally) critical. We identify four main features, i.e., the two local maxima (the ‘first’ in the lower left quadrant of the field, and the ‘second’ at the boundary between the lower left and lower right quadrant), the overall increase of  $\kappa_\infty$  towards the first maximum in the lower two quadrants, and a minimum in the upper right quadrant.

In Fig. 6 we show the mass density distributions corresponding to the four shear fields presented in Fig.3 assuming the redshift distribution (3.8) with  $\beta = 1$  and  $\langle z \rangle = 0.8$ . As expected from the shear fields, the mass distribution does not change dramatically. We find an overall decrease in the mass density for the brighter galaxy samples from  $R \in (23, 25.5)$  to  $R \in (21, 25.5)$ . However, the faintest sample with  $R \in (24, 25.5)$  gives a mass distribution with a slightly smaller maximum than that of  $R \in (23, 25.5)$ . We think that this is not significant and may be due to the fact that fewer images are used.

To investigate the stability of the reconstructed mass distribution, we repeat the reconstruction for the same parameters  $\langle z \rangle = 1$  and  $\beta = 1$  as used for the reconstruction shown in the lower left panel of Fig.5 ( $s = 0.3$ ), but vary the smoothing length. The results are shown in Fig.7 for  $s = 0.2$  (upper left),  $s = 0.25$  (upper right),  $s = 0.35$  (lower left) and  $s = 0.4$  (lower right). We find that independent of the smoothing length all main features can be recovered. Obviously, a smoothing length  $s = 0.2$  gives a too

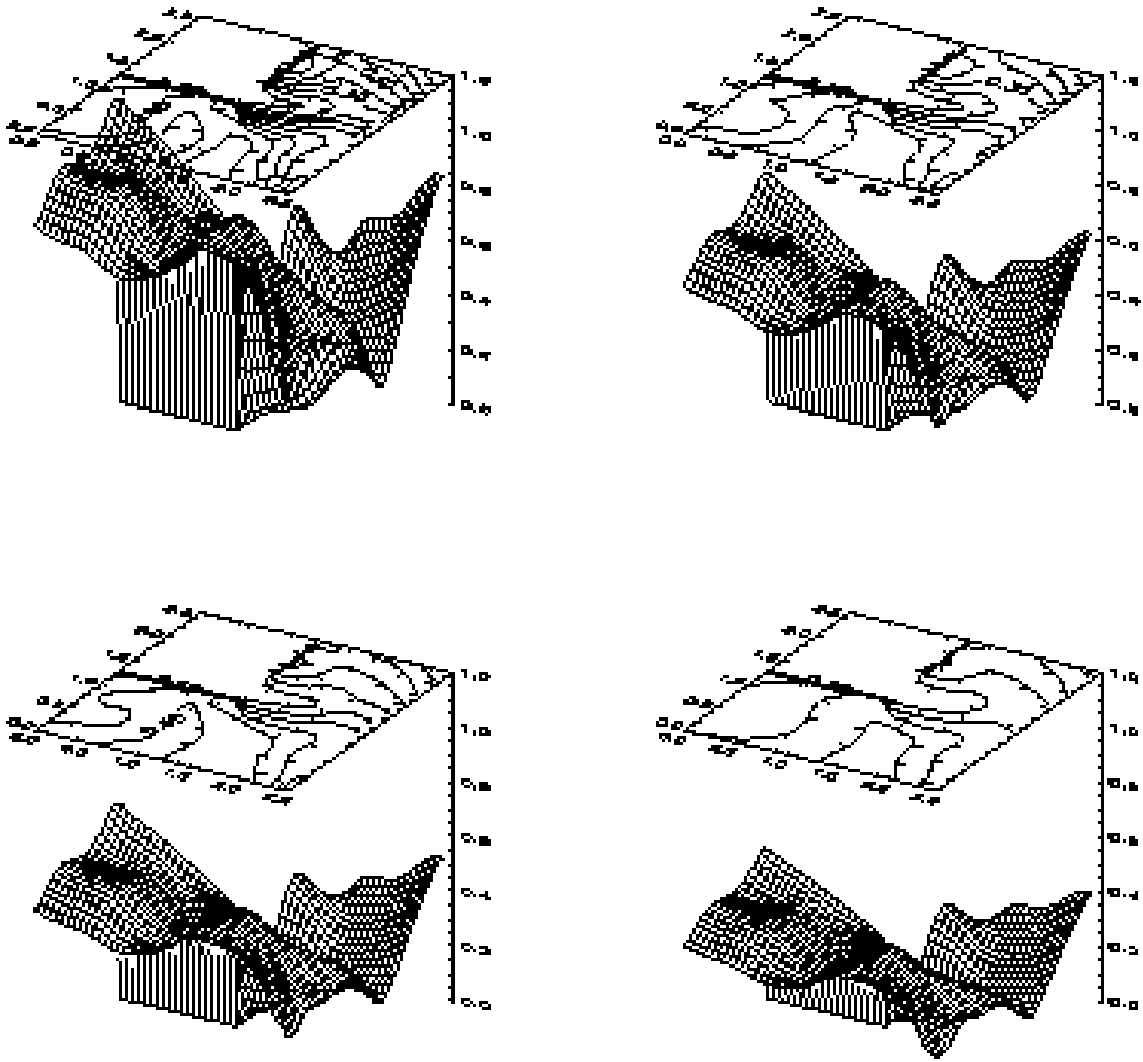


**Fig. 5.** The reconstructed surface mass density of the cluster CL 0939+4713. For the reconstruction we use 295 galaxy images with  $R \in (23, 25.5)$  and assume that their redshift distribution is given through (3.8) with  $\beta = 1$  and  $\langle z \rangle = 0.6$  (upper left),  $\langle z \rangle = 0.8$  (upper right),  $\langle z \rangle = 1$  (lower left) or  $\langle z \rangle = 1.5$  (lower right). For all these reconstructions we use a smoothing length of  $s = 0.3$  in the weight function appearing in Eq.(2.2). Since we use no data on the upper left quadrant, and therefore cannot reconstruct the surface mass density there, we arbitrarily set  $\kappa = 0$  in this quadrant; this leads to the ‘funny’ shape in the level plots and the jumps in the corresponding contour plots, which are seen throughout this paper. The small discontinuity along the diagonal of the lower right quadrant is due to joining together two independent reconstructions, as described in the text

noisy reconstruction, whereas  $s = 0.4$  may smooth out too much of the structure. From visual inspection we decided to use a smoothing length of  $s \approx 0.3$  in the remainder of this paper. We would like to note that a fixed smoothing length is not necessarily the best choice, but a smoothing length, adapted to the local signal strength, may be more appropriate. Such a local adaption can be objectively controlled with local  $\chi^2$ -statistics, or by using regularized maximum-likelihood inversion techniques (Bartelmann et al. 1995).

As a further check for the stability and reliability of the reconstructed mass distribution, we perform a bootstrap analysis: we use the data set consisting of the position-vectors and ellipticities of the  $N_{\text{gal}} = 295$  faint background galaxies with  $R \in (23, 25.5)$

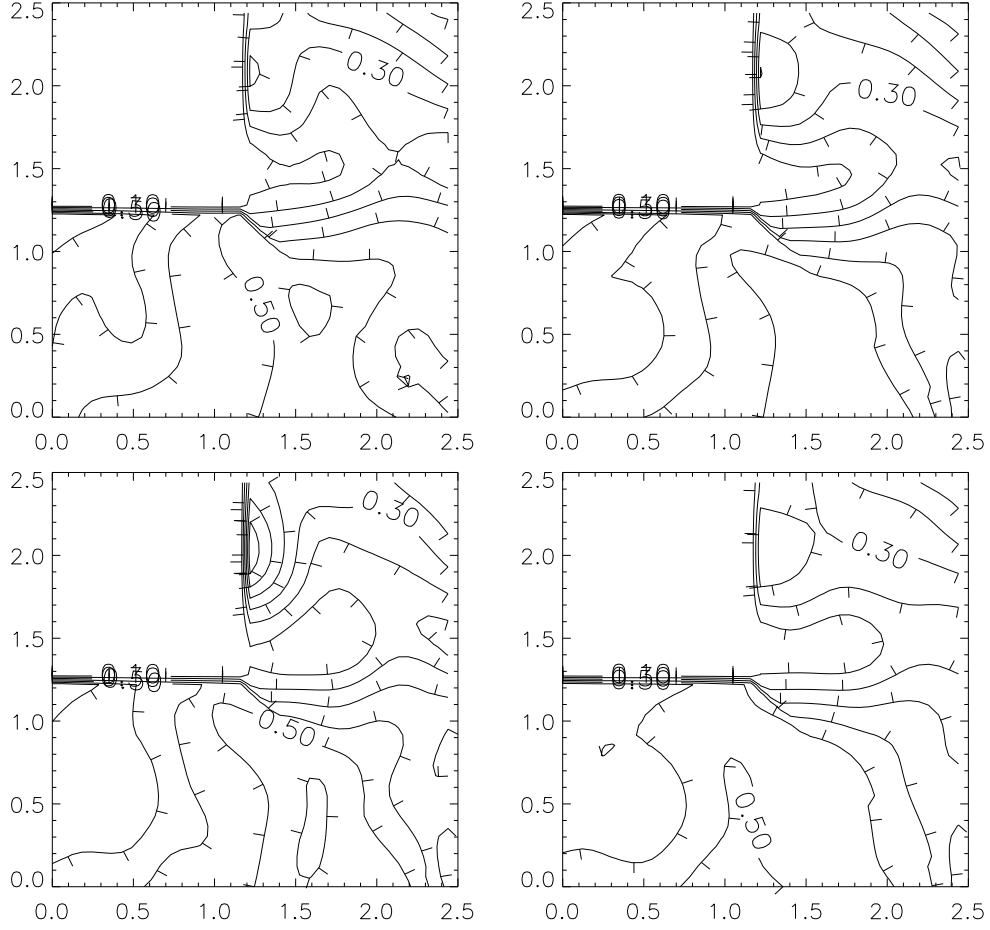


**Fig. 6.** The reconstructed surface mass density obtained for the galaxy samples corresponding to the shear field shown in Fig. 3:  $R \in (24, 25.5)$  (upper left),  $R \in (23, 25.5)$  (upper right),  $R \in (22, 25.5)$  (lower left) and  $R \in (21, 25.5)$  (lower right). For all four reconstructions we assume that the redshift distribution is given through (3.8) with  $\beta = 1$  and  $\langle z \rangle = 0.8$

and generate a number of synthetic data sets by drawing  $N_{\text{gal}}$  galaxies at a time with replacement from the original data set. For each of the synthetic data sets we perform the mass reconstruction. Mass distributions from three different bootstraps are shown in the upper left, upper right and lower left panels of Fig. 8. Taking into account that in the bootstrap analysis on average  $1/e \approx 36\%$  of all galaxies are not used at all, the fact that the main features are still recovered increases our confidence in the reconstruction. The average mass density of 30 bootstraps, shown in the lower right panel of Fig. 8, is very similar to the mass distribution shown on the lower left of Fig. 5, where all galaxies and the same smoothing length  $s = 0.3$  are used. Comparing the mass reconstructions obtained from different bootstrapping realizations, one can see that the relative variations are considerably larger near the boundary of the data field. This is due to the fact that a point on the boundary has fewer neighboring galaxies, and thus takes into account less information of the local shear. We want to stress, however, that this is a ‘random’ noise components, and not a systematic boundary effect.

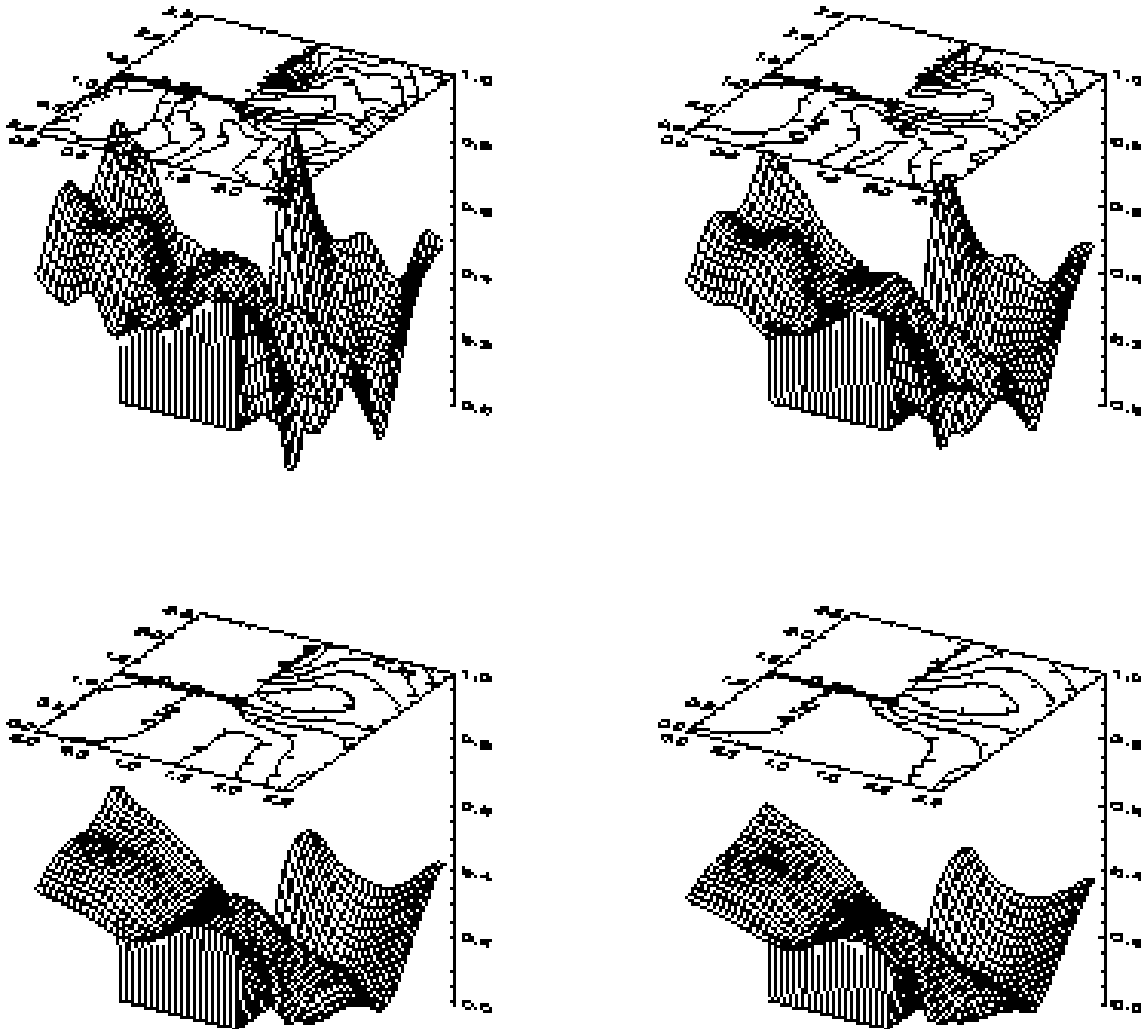


**Fig. 7.** The reconstructed surface mass density for different values of the smoothing length  $s$ , with  $\langle z \rangle = 1$  and  $\beta = 1$ . For the upper left panel we use  $s = 0.2$ , for the upper right  $s = 0.25$ , for the lower left  $s = 0.35$  and for the lower right  $s = 0.4$ . Note that the main features are common to all mass distributions shown

## 4.2 Correlation between mass and light

We want to compare the reconstructed mass distribution with the light distribution of different samples of galaxies. For this we calculate the gaussian-smoothed light distribution via

$$\sigma_{\text{light}}(\boldsymbol{\theta}) = \frac{\sum_{k=1} \exp\left(-\frac{|\boldsymbol{\theta} - \boldsymbol{\theta}_k|^2}{s^2}\right) 10^{-0.4(m_k - 20)}}{\int_{\mathcal{U}} d^2\theta' \exp\left(-\frac{|\boldsymbol{\theta} - \boldsymbol{\theta}'|^2}{s^2}\right)}, \quad (4.1)$$

where  $\mathcal{U}$  is the data field (i.e. the three quadrants),  $\boldsymbol{\theta}_k$  and  $m_k$  are the positions and magnitudes of the galaxies used, and a smoothing scale of 0.3 is used. The denominator in (4.1) corrects for boundary effects.

In Fig. 9a we show the light distribution of all galaxies [roughly  $r \in (17, 23)$ ] detected by Dressler & Gunn (1992) on a field of  $4' \times 4'$ . Comparing this with the mass distribution shown in Fig. 5 & 6 we detect a remarkable correlation: the position of the maximum in

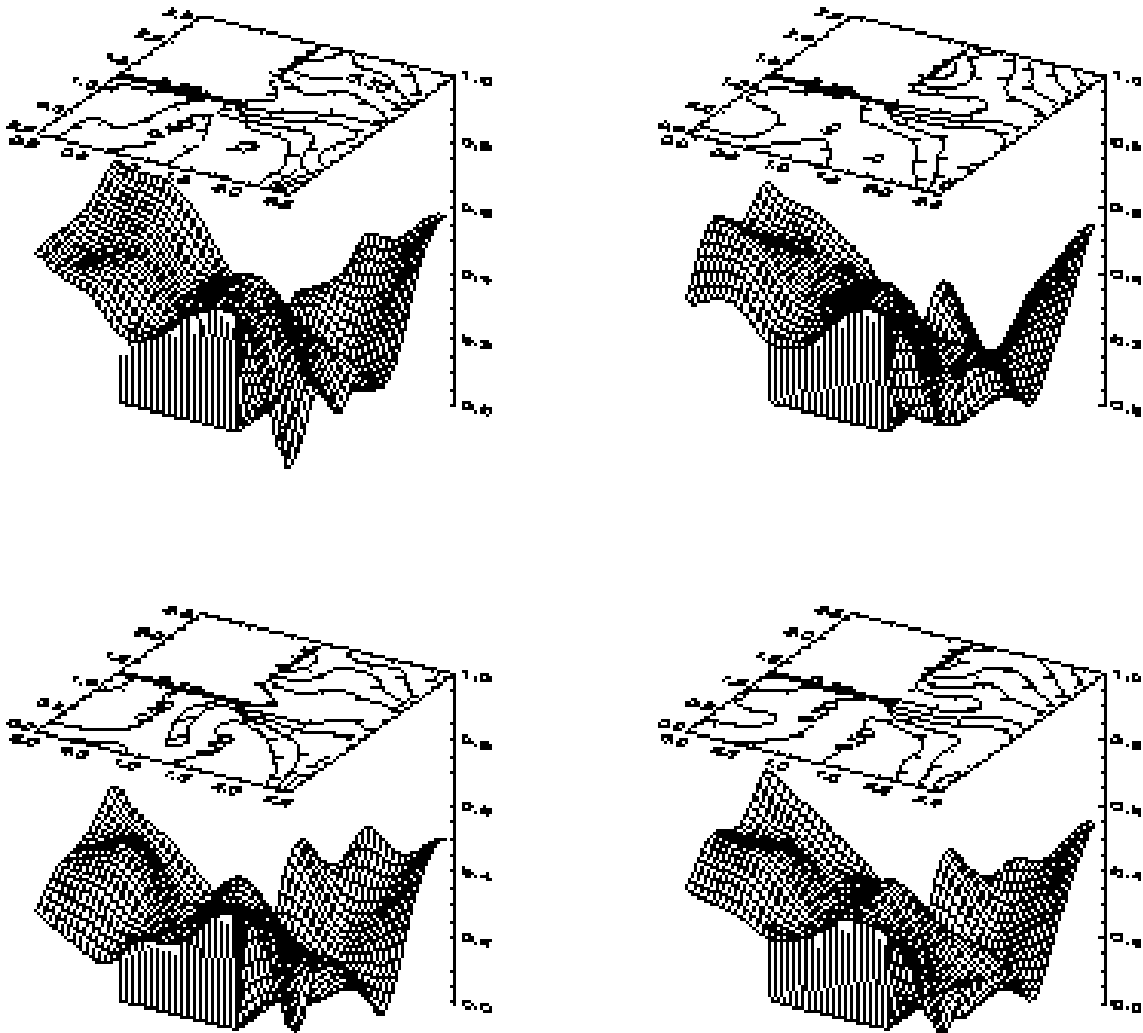


**Fig. 8.** Three mass distributions (upper left and right, lower left) resulting from different bootstrapping realizations (see text) for  $\langle z \rangle = 1$ ,  $\beta = 1$  and  $s = 0.3$ . The lower right panel shows the average of 30 bootstrapping mass distributions

the mass density corresponds reasonably well with the position of the maximum in the light distribution, which is approximately located there where Dressler & Gunn (1992) proposed the cluster center. The secondary mass maximum corresponds to a group of bright galaxies. It is more prominent in the light than in the mass distribution and displaced slightly to the left relative to the position of the secondary maximum in the mass. The minimum of the mass distribution corresponds to a region where very few bright galaxies are observed.

Dressler et al. (1994b) studied the morphology of the bright (cluster) galaxies with the HST (WFPC1); we show in Fig. 9b the light distribution of their identified E/S0 galaxies, tracing the old cluster galaxy population. The position of the secondary maximum in this light distribution corresponds better with the position of the secondary mass maximum and the correspondence with the other features is as good. Hence we conclude that there is a correlation between the reconstructed mass distribution and the light distribution of the bright galaxies, which are mostly cluster galaxies.

To investigate the correlation between mass and light more quantitatively, we calculate from each mass distribution  $\kappa_\infty(\theta)$  obtained in a bootstrap realization (see Sec. 4.1)

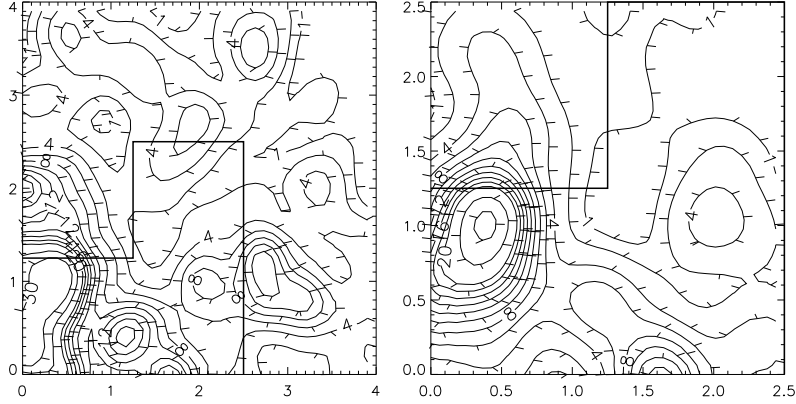


**Fig. 9.** (a) The gaussian-smoothed light distribution defined through Eq. (4.1) of all galaxies [roughly with  $r \in (17, 23)$ ] detected by Dressler & Gunn (1992) on a field of  $4' \times 4'$ . We use a smoothing length  $s = 0.3$ . (b) The gaussian-smoothed light distribution of all E/S0 galaxies identified in the field of about  $2.5 \times 2.5$  [WFPC1, Dressler et al. (1994b)]. The area covered by the HST (WFPC2) observations is indicated by the solid lines

the number

$$V := \frac{\sum_{\text{galaxies}} [\kappa_{\infty}(\boldsymbol{\theta}_{\text{galaxy}}) - \langle \kappa_{\infty} \rangle]}{N}, \quad (4.2)$$

for different samples of  $N$  galaxies, where  $\langle \kappa_{\infty} \rangle$  is the average of  $\kappa_{\infty}$  over our data field  $\mathcal{U}$ . If the galaxies were randomly distributed, the expectation value of  $V$  would be zero, whereas a positive (negative) correlation of galaxies with the reconstructed mass density is indicated by  $V > 0$  ( $V < 0$ ).

From 1000 bootstrap realizations we find the distributions  $p(V)$  shown in Fig. 10a for the E/S0 galaxies identified by Dressler et al. (1994b) (DG: E/S0: dashed curve), all galaxies detected from the WFPC2 data regardless from their size (solid curve) and all galaxies with  $R \in (24, 25.5)$  (dotted curve) – also regardless of size. Clearly, a strong positive correlation between the reconstructed mass and the DG:E/S0 galaxies is detected. Next, a weaker positive correlation between ‘all’ galaxies and the mass distribution, and an anti-correlation between the mass distribution and the faint galaxies [ $R \in (24, 25.5)$ ] is visible. This anti-correlation appears surprising on first sight, as certainly some of the faint galaxies belong to the cluster, and, as we have argued above, the cluster galaxies are positively correlated with the mass. To investigate this point further, we have calculated the distribution of  $V$  for the same magnitude interval, but leaving out the lower left CCD where the contribution from cluster galaxies is expected to be strongest. The resulting distribution is also plotted in Fig. 10a, indicated with an asterisk; it shows an even stronger anti-correlation.

In Fig. 10b we show the mean correlation coefficient  $\langle V \rangle$  from 1000 simulations as a function of the magnitude range of the galaxies. We find that  $\langle V \rangle$  is strongly correlated with the faintness of the magnitude interval  $(m_1, m_2)$  chosen. It decreases towards the fainter samples and eventually becomes negative. This is due to the larger fraction of background galaxies contributing to the counts in  $(m_1, m_2)$  for fainter slices.

We now turn to a possible explanation for the anti-correlation of the faint galaxies with the reconstructed surface mass density:

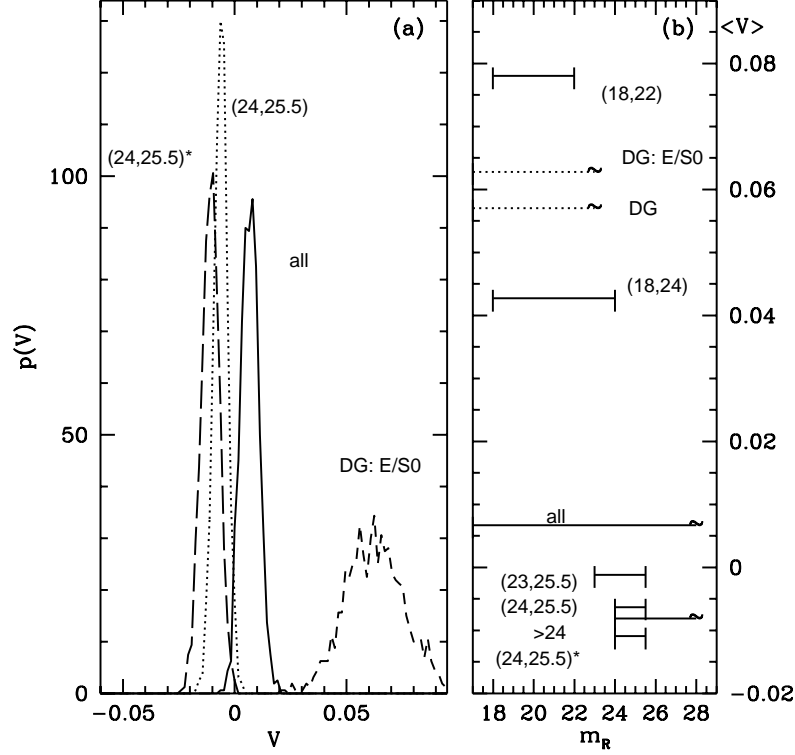


**Fig. 10.** (a): The normalized distribution  $p(V)$  of the quantity  $V$  defined in Eq. (4.2), calculated from reconstructed mass distributions for 1000 bootstrap data sets drawn from the observed one ( $R \in [23, 25.5]$ ) with replacement. The solid curve shows the distribution for all galaxies detected from the WFPC2 observations, the dotted curve for all galaxies with  $R \in [24, 25.5]$ , the long dashed curve for all galaxies detected in the two right CCD frames with  $R \in [24, 25]$  and the dashed curve for E/S0 galaxies identified Dressler et al. (1994b). (b): The mean correlation coefficient  $\langle V \rangle$  for different galaxy samples chosen. The tilde indicates that the subsample has no well-determined flux threshold

The locally observed number density  $n_L(> S)$  of lensed background galaxies with flux larger than  $S$  is related the unlensed number density  $n_0(> S)$  through the local magnification  $\mu$  caused by the cluster,

$$n_L(> S, \boldsymbol{\theta}) = \frac{1}{\mu(\boldsymbol{\theta})} n_0\left(> \frac{S}{\mu(\boldsymbol{\theta})}, \boldsymbol{\theta}\right), \quad (4.3)$$

where

$$\mu(\boldsymbol{\theta}) = \int_0^\infty dz p_s(z) \frac{1}{|[1 - w(z)\kappa_\infty(\boldsymbol{\theta})]^2 - w(z)^2\gamma_\infty^2(\boldsymbol{\theta})|}, \quad (4.4)$$

is the redshift-averaged local magnification, weighted by the redshift distribution of the galaxies. The first factor in (4.3) is due to the increase of the solid angle, whereas the argument of  $n_0$  indicates that a magnified source can be ‘intrinsically’ fainter by a factor  $\mu$  and still be included in a flux-limited sample. Which of the two competing processes wins depends on the slope  $n_0(> S)$  of the sources. The observed galaxy counts in the R-band shows that it is well fitted by  $N(R) \propto 10^{\gamma R}$  with  $\gamma = 0.32$ . Therefore, we obtain from Eq.(4.3)

$$\frac{n_L(> S)}{n_0(> S)} = \mu^{2.5\gamma-1} . \quad (4.5)$$

The magnification (see also Broadhurst, Taylor & Peacock 1995, hereafter BTP) can be obtained via

$$\mu = \left[ \frac{n_L(> S)}{n_0(> S)} \right]^\alpha \quad \text{with} \quad \alpha = \frac{1}{2.5\gamma-1} . \quad (4.6)$$

For  $\gamma = 0.32$ , the exponent in Eq. (4.6) is  $\alpha = -5$  and a suppression of background galaxies is expected in regions of high magnifications, or high surface mass density.

In Fig. 11 we show the gaussian-smoothed number density [defined as in (4.1) without flux weighting] of the faint galaxies with  $R \in (24, 25.5)$ . We see a local maximum where we detect the minimum of the mass, indicating that we found the expected anti-correlation. However, we also find two local maxima in the number density of the faint objects where we detect the maxima of the mass. Note that we have not corrected the faint galaxy density for occupation of some CCD area by bright (cluster) galaxies, which is of course strongest near the cluster center; this shows that the contribution of cluster members to the faint galaxy counts is slightly stronger than indicated by comparing Fig. 11 with Fig. 9. We thus conclude that a non-negligible fraction of the faint galaxies are cluster members, as also follows from Fig. 2.

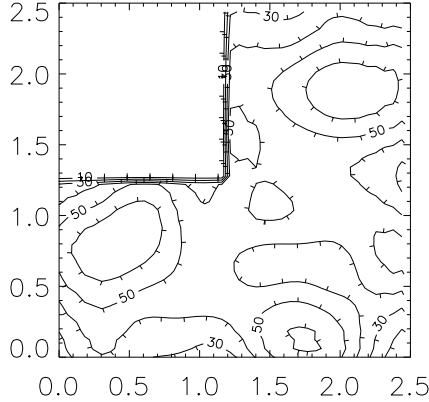


**Fig. 11.** The gaussian-smoothed number density of the faint galaxies with  $R \in (24, 25.5)$ . We use a smoothing length  $s = 0'.3$

Assuming that the cluster galaxies have an average correlation coefficient  $\langle V \rangle_c > 0$  with the mass distribution, independent of the magnitude of the galaxies, and that the background galaxies have an average correlation coefficient  $\langle V \rangle_b < 0$ , again independent of their magnitudes, one can then derive the fraction  $x$  of cluster galaxies in a magnitude slice  $(m_1, m_2)$  through measuring

$$\langle V \rangle_{m_1, m_2} = x \langle V \rangle_c + (1 - x) \langle V \rangle_b .$$

Using  $\langle V \rangle = \langle V \rangle_c$  from the galaxies with  $R \in (18, 22)$  and  $\langle V \rangle_b$  from the galaxies with  $R \in (24, 25.5)$ \* we estimate the fraction of cluster galaxies to be 83% for the ‘DG E/S0’ sample, 76% for the DG sample, 60% for the galaxies with  $R \in (18, 24)$ , 11% for  $R \in (23, 25.5)$  and 5% for  $R \in (24, 25.5)$ . Of course these values are crude estimates only, but they do not appear unreasonable.



To summary this subsection, the correlation of bright galaxies with the reconstructed surface mass density shows that *in this cluster ‘mass follows light’ on average*. Hence, *overdensities of bright galaxies correspond to local maxima in the projected mass density*. The also significant anti-correlation of faint galaxies with the reconstructed mass profile is most likely an effect of the magnification (anti)bias, which has been pointed out by Broadhurst, Taylor & Peacock (1995) and which was detected in the cluster A1689 (Broadhurst 1995).

### 4.3 Limits on the mass inside the data field

Requiring that the surface mass density can not be negative one can obtain a lower limit on the mass inside the data field by applying the invariance transformation (3.5) such that the minimum of the resulting  $\kappa_\infty$ -map is zero. Using the galaxies with  $R \in (23, 25.5)$ , we find as a *lower bound* on the total mass inside the data field (side length about 1 Mpc  $h_{50}^{-1}$ ) about  $M/(10^{14}h_{50}^{-1}M_\odot) \geq 6.3$  (4.3, 3.6, 2.8) for a mean redshift  $\langle z \rangle = 0.6$  (0.8, 1.0, 1.5). These limits depend only slightly on the actual form of the assumed redshift distribution, as shown in Fig.12.

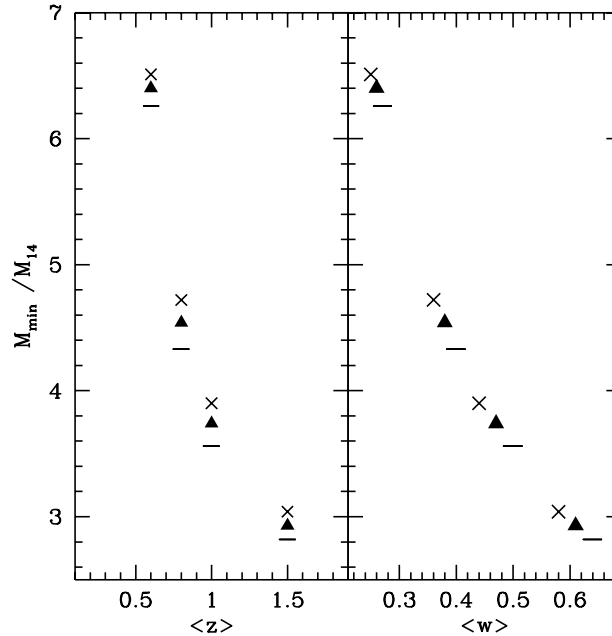


**Fig. 12.** Lower limits  $M_{\min}$  on the total mass inside the data field in units of  $M_{14} = 10^{14}h_{50}^{-1}M_\odot$  as a function of the assumed mean redshift  $\langle z \rangle$  (left) or the mean  $\langle w \rangle$  (right) of the images used for the reconstruction, assuming the redshift distribution (3.8). Crosses show the results for  $\beta = 1$ , triangles for  $\beta = 1.5$  and dashes for  $\beta = 3$ . The smoothing length is  $s = 0'.3$

The most conservative *upper limit* of the mass we can give is  $M < 10^{15}h_{50}^{-1}M_\odot$ , because this corresponds to  $\langle \kappa_\infty \rangle = 1$  and would most probably produce several giant arcs which are not observed.

Using Eq. (4.6), one can in principle derive the local magnification  $\mu(\theta)$  and could therefore break the global invariance transformation (3.5) with the measurement of  $\mu(\theta)$

at one particular point in the cluster. However, in practice we have the following difficulties: (1) since lensing effects are nowhere weak on the whole field we have no measurement of  $n_0(> S)$ ; (2) we have no colour information of the galaxies and therefore we can not well distinguish between faint cluster galaxies and lensed background galaxies; (3) possible clustering of background objects and confusion with cluster member galaxies leads to a high noise in the estimate of  $\mu(\theta)$  and a poor resolution. Therefore, we can not derive an accurate high-resolution map of the magnification from Eq. (4.6).

Nevertheless, we can use the magnification (anti) bias to derive (crude) estimates of the total mass inside the data field. Crucial for this is the assumption that the unlensed number counts  $n_0(> S)$  can be taken from the literature. We use the amplitude and slope given in Smail et al. (1995b) which gives for the data field  $\mathcal{U}$  and galaxies with  $R \in (23, 25.5)$   $N_0(23, 25.5) = 278$ . The observed number of  $N^{\text{obs}}(23, 25.5) = N^{FG} + N^{CG} = 295$  is a sum of cluster galaxies (CG) and galaxies belonging to the faint galaxy field population (FG). Now, we assume that a fraction  $x$  of the observed galaxies  $N^{\text{obs}}$  are cluster galaxies and obtain

$$\langle \mu^{2.5\gamma-1} \rangle_{\mathcal{U}} = \frac{N^{FG}}{N_0} = \frac{(1-x)N^{\text{obs}}}{N_0}. \quad (4.6)$$

For  $x = 0.15$  (0.2) we obtain  $\langle \mu^{2.5\gamma-1} \rangle_{\mathcal{U}} = 0.849$  (0.796). We perform the reconstruction assuming a value of  $\lambda$ , or equivalently, a value of  $\langle \kappa_{\infty} \rangle$ , and calculate from the resulting mass map  $\kappa_{\infty}$  and the shear map  $\gamma_{\infty}$  locally the expectation value of the magnification (4.4) of the sources and finally average  $\mu^{2.5\gamma-1}$  on the field  $\mathcal{U}$  to obtain  $\langle \mu^{2.5\gamma-1} \rangle_{\mathcal{U}}$ . Next, we search for that value of  $\langle \kappa_{\infty} \rangle$  which gives the value  $\langle \mu^{2.5\gamma-1} \rangle_{\mathcal{U}}$  corresponding to a certain fraction  $x$  of cluster galaxies. In Fig. 13 we show the mass estimates for  $x = 0.15$  (solid curve) and  $x = 0.2$  (dotted curve) as a function of the assumed mean redshift of the galaxies used for the reconstruction. For comparison we show again the minimum mass (dashed curve) as shown in Fig. 12 for  $\beta = 1$ . From these lower limits on the mass we conclude that the fraction of cluster galaxies in the galaxy sample with  $R \in (23, 25.5)$  is  $x \gtrsim 0.1$ .

We note that recently we became aware of a paper by Belloni et al. (1995) which could allow for a better separation between cluster and background galaxies for the galaxies with  $R \in (23, 25.5)$ : Belloni et al. used multiband photometry to get the redshifts of 275 bright galaxies with  $R < 22.5$ , i.e., the fraction of cluster galaxies in the sample of galaxies with  $R < 22.5$ . From that and the known slope of the faint field galaxies, we can probably derive a better estimate for the fraction of cluster galaxies in the faint galaxy sample with  $R \in (23, 25.5)$ .

#### 4.4 The mass to light ratio

We calculate the total light of all galaxies inside the field  $\mathcal{U}$  detected by Dressler et al. (1994b) leaving aside those galaxies whose measured redshift exclude a cluster membership. Magnitudes for these galaxies are given in gunn-r ( $\bar{\lambda} = 655$  nm), which correspond to a rest-frame wavelength of  $\lambda \approx 464$  nm), i.e. the measured  $r$  magnitudes correspond to the  $B$  ( $\bar{\lambda} = 443$  nm) magnitudes in the rest-frame. As a result we obtain for this sample a total luminosity of  $(L/L_{\odot})_B = 5 \times 10^{12} h_{50}^{-2}$ . From this and the mass estimates shown in Fig. 13 we derive the  $M/L$  values shown in Fig. 14. If the Dressler et al. (1994b) sample of galaxies with  $r \in (17, 23)$  represents the luminosity of cluster galaxies well and

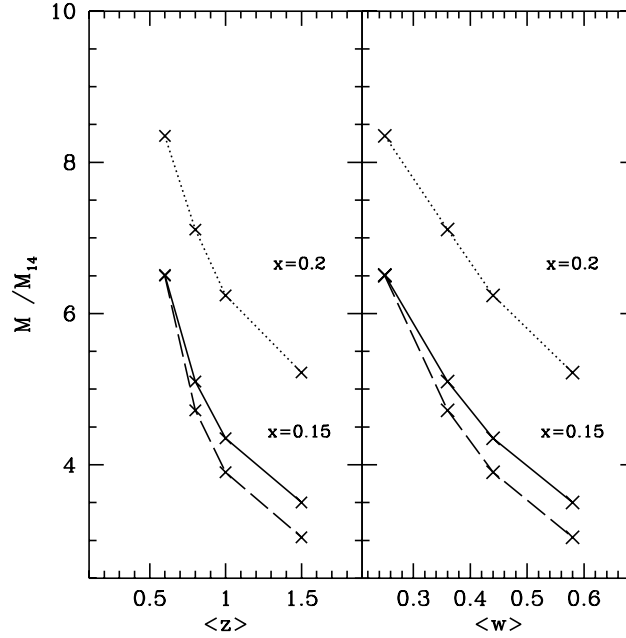


**Fig. 13.** The mass  $M$  inside the data field in units of  $M_{14} = h_{50}^{-1} 10^{14} M_{\odot}$  as a function of the assumed mean redshift  $\langle z \rangle$  (left) or the mean  $\langle w \rangle$  (right) of the images used for the reconstruction, assuming the redshift distribution (3.8) with  $\beta = 1$ . The solid curve shows the total mass in the field  $\mathcal{U}$  assuming that  $x = 15\%$  of all galaxies detected within  $R \in (23, 25.5)$  are cluster galaxies, the dotted curve shows the result for  $x = 20\%$ . For comparison we show  $M_{\min}$  from Fig. 12 (dashed curve)

if the mean redshift of the faint galaxies [ $R \in (23, 25.5)$ ] used for the mass reconstruction is  $\langle z \rangle = 0.8$ , then we derive from the non-negativity of the surface mass density a lower limit on  $M/L \gtrsim 93h_{50}$  (dashed curve in Fig. 14) for the cluster CL0939+4713, and the values  $M/L \approx 102h_{50}$  for a fraction of  $x = 0.1$  of cluster galaxies in the faint galaxy sample (solid curve) and  $M/L \approx 142h_{50}$  for  $x = 0.2$  (dotted curve). From the absence of giant luminous arcs we derive - independently of the assumed redshift of the sources or the fraction of cluster galaxies - a robust upper limit  $M/L \lesssim 200h_{50}$ . Of course, the sample chosen for calculating the luminosity of the cluster includes a certain fraction of background- and foreground galaxies, but this is partly compensated because we will miss a certain fraction of faint cluster galaxies. To derive a conservative upper limit of the total luminosity of the cluster, or a conservative lower limit on  $M/L$  we calculate the total luminosity of all galaxies detected in the field (down to  $R = 26.5$ ) and obtain almost twice the value  $(L/L_{\odot})_B$  found above, or half the values for  $M/L$  as shown in Fig. 14.

The fact that the  $M/L$  values (see Fig. 14) are small compared to the  $M/L$  found for other cluster from a weak lensing analysis (see Fahlman et al. (1994), or Smail et al. (1995a)), is not too surprising taking into account that CL0939+4713 is an *optically* selected (Abell) cluster with high redshift  $z_d = 0.41$ . A moderately bright cluster at this redshift would probably not have entered the Abell catalog. In addition, the  $M/L$ -ratio quoted here is uncorrected for cosmic evolution, which can be quite substantial from  $z = 0.4$  to today in the B-band, so that the corresponding  $M/L$  value ‘today’ would be

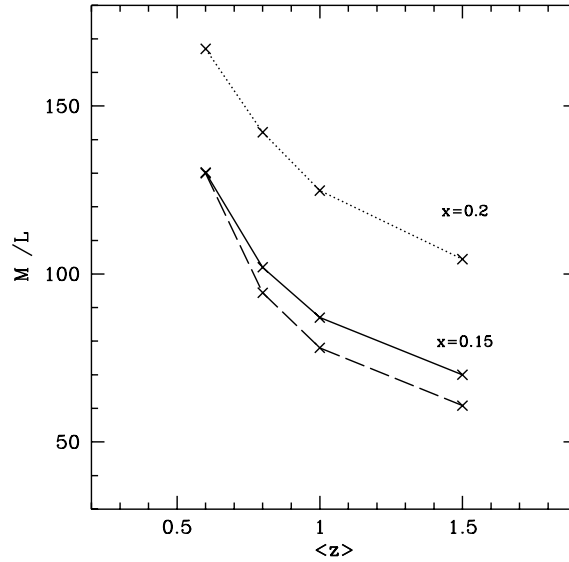


**Fig. 14.** The values of  $(M/L)_B$  in units of  $h_{50}(M_\odot/L_\odot)_B$  obtained for the masses shown in Fig. 13. To calculate the luminosity  $L$  we used all galaxies identified by Dressler & Gunn (1992) in that field, excluding those galaxies for which a measured redshift shows that they are no cluster members

considerably higher.

#### 4.5 The Rosat PSPC image

In Fig. 15 we show the Rosat PSPC image of the cluster obtained from a gaussian smoothing of the counts with a smoothing length of  $s = 0'.2$ . The center of the coordinate frame coincides with the lower left corner of the HST image shown in Fig. 1. To align the PSPC image with the HST image we used a star. Thus, the alignment should be better than one PSPC pixel (pixelsize  $15''$ ). The PSPC image shows a main X-ray emission around the cluster center, which roughly corresponds to the region where we derive a maximum of the light and a maximum of the mass distribution. The PSPC data are analysed in a forthcoming paper by S. Schindler. In order to perform a more detailed comparison between the X-ray and mass distribution one has to wait for the ROSAT HRI image.

**Fig. 15.** The PSPC image of the cluster CL0939+4713. The contour-lines show the photon counts, ranging from 9.5 down to 1.5 with a spacing of 1. North is at the bottom and east to the right

## 5 Discussion

Using deep WFPC2 data, we have reconstructed the projected (dark) matter distribution of the cluster CL0939+4713. The distortion of faint background galaxies was used to construct a ‘shear map’ of the cluster, from which an unbiased, nonlinear estimate of the surface mass density was constructed. The resulting mass map is defined up to an overall invariance transformation, a generalization of the so-called mass sheet degeneracy. The mass distribution is strongly correlated with the projected distribution of the bright cluster galaxies; in particular, the maximum of the mass map coincides with the cluster center as determined from the light distribution, a secondary maximum of the map corresponds to a concentration of cluster galaxies, and a deep mass minimum occurs where the number density of cluster galaxies is lowest. We also note that the main mass (and light) maximum correspond to maximum in the X-ray emission, as seen with the ROSAT PSPC. The anti-correlation of mass with faint galaxies is interpreted as the difference between a positive correlation of mass with faint cluster galaxies (mainly seen towards the cluster center), and a magnification anti-bias (BTP), which is expected due to the flatness of the galaxy number counts.

Our analysis shows that the recently developed cluster inversion techniques can be applied to (sufficiently deep) WFPC2 data (in order to image precisely faint galaxies), despite the fact that its field-of-view is fairly limited. It is *essential* to use an unbiased finite-field inversion technique in this case, and also, since the cluster center is (nearly) critical, to account for strong lensing effects. Also, owing to the fairly large redshift of the lensing cluster, the redshift distribution of the background galaxies has to be taken into account explicitly; only in weak lensing regime does this distribution not enter the reconstruction, but only the mean of the distance ratio  $D_{ds}/D_s$ .

We have checked the robustness of the mass reconstruction, by using different magnitude cuts for the galaxies and by extended bootstrap simulations. *The main features of the mass map – the two mass maxima, the pronounced minimum, and the overall gradient toward the cluster center – are stable.* The anti-correlation of mass with the faint galaxies, and the strong correlation with cluster galaxies, further increases our confidence in the reconstruction. We have derived estimates of the cluster mass contained within the WFC aperture, which depend on the assumed redshift of the background galaxies. A robust lower limit of the mass follows from the non-negativity of the surface mass density, a robust upper limit comes from the absence of giant luminous arcs. To derive a narrower mass range, one needs to fix the parameter  $\lambda$  contained in the invariance transformation (3.5). This can be done by using the magnification anti-bias (BTP). In the only case where this effect has been demonstrated before (A1689, Broadhurst 1995), a color criterium was used to ensure that the galaxies are likely background galaxies. Since we lack color information, the fraction of the faint galaxies which are cluster members or foreground galaxies cannot be separated from background galaxies. Nevertheless, a plausible range for  $\lambda$  can be obtained and led to the mass estimates shown in Fig. 13.

The exploration of this novel method to reconstruct the density distribution of clusters has only just begun. In contrast to current ground-based data, for which image ellipticities have to be substantially corrected for seeing effects, WFPC2 data provide relatively ‘clean’ probes of image ellipticities. The small field of view of WFPC2 limits the extent to which clusters can be mapped (specially for nearby clusters), unless mosaics are taken, but high-resolution mass maps such as the one constructed here are invaluable tools for investigating substructure in cluster mass distributions and their relation to substructure in the distribution of galaxies and X-ray emission.

*Acknowledgement.* CS would like to thank Hans-Walter Rix for many useful discussion and for introducing her to the IRAF software package and Sabine Schindler for help concerning the PSPC data. We gratefully acknowledge enthusiastic discussion with Ian Smail, Richard Ellis, Yannick Mellier and Bernard Fort on cluster-lenses. This work was supported by the “Sonderforschungsbereich 375-95 für Astro-Teilchenphysik” der Deutschen Forschungsgemeinschaft. JPK acknowledges support from a HCM-EU fellowship and the hospitality of the MPA during a visit when this project was started.

## References

- Bartelmann, M. 1995, A&A, 303, 643.
- Bartelmann, M. & Narayan, R. 1995, ApJ, 451, 60.
- Bartelmann, M., Narayan, R., Seitz, S. & Schneider, P. 1995, submitted to ApJ.
- Bertin & Arnouts 1995, A&A submitted.
- Belloni, P., Bruzual, A.G., Thimm, G.J. & Röser, H.J. 1995, 297, 61
- Bonnet, H., Mellier, Y. & Fort, B. 1994, ApJ 427, L83.
- Brainerd, T.G., Blandford, R. & Smail, I. 1995, preprint.
- Broadhurst, T.J., Taylor, A.N. & Peacock, J.A. 1995, ApJ 438, 49.

- Broadhurst, T.G. 1995, preprint.
- Coless, M., Ellis, R.S., Broadhurst, T.J., Taylor, K. & Peterson, B. 1993, MNRAS 261, 19.
- Cowie, L.L., Hu, E.M. & Songaila, A. 1995, accepted for Nature.
- Dressler, A. & Gunn, J.E. 1992, ApJSS, 78, 1.
- Dressler, A., Oemler, A., Sparks, W.B. & Lucas, R.A. 1994a, ApJ 435, L23.
- Dressler, A., Oemler, A., Butcher, H. & Gunn, J.E. 1994b, ApJ 430, 107.
- Fahlman, G.G., Kaiser, N., Squires, G. & Woods, D. 1994, ApJ 437, 63.
- Fort, B. & Mellier, Y. 1994, A&AR 5, 239.
- Gorenstein, M.V., Falco, E.E. & Shapiro, L.I. 1988, ApJ 327, 693.
- Holtzman, J.A., Burrows, C.J., Casterno, S., Hester, J.J., Trauger, J.T., Watson, A.M., Worthey, G., 1995, preprint.
- Kassiola, A., Kovner, I., Fort, B. & Mellier, Y. 1994, ApJ 429, L9.
- Kaiser, N. & Squires, G. 1993, ApJ 404, 441 (KS).
- Kaiser, N. 1995, ApJ 493, L1.
- Kaiser, N., Squires, G., Fahlman, G.G., Woods, D. & Broadhurst, T. 1994, preprint astro-ph/9411029.
- Kneib, J.P., Ellis, R.S., Smail, I.R., Couch, W.J., Sharples, R., 1995, ApJ submitted.
- Kochanek, C.S. 1990, MNRAS 247, 135.
- Lilly, S. 1993, ApJ 411, 501.
- Miralda-Escude, J. 1991, ApJ 370, 1.
- Schneider, P. 1995, A&A, in press.
- Schneider, P. & Seitz, C. 1995, A&A 294, 411.
- Smail, I., Ellis, R.S., Fitchett, M.J. 1995a, MNRAS 273, 277.
- Smail, I., Hogg, D.W., Yan, L. & Cohen, J.G. 1995b, ApJ, 449, L105.
- Seitz, C. & Schneider, P. 1995a, A&A 297, 287.
- Seitz, C. & Schneider, P. 1995c, in preparation.
- Seitz, S. & Schneider, P. 1995b, A&A, in press.
- Tyson, J.A., Valdes, F. & Wenk, R.A. 1990, ApJ 349, L1.